PCCP

Potential energy surface for high-energy N + N2 collisions

Journal:	*Physical Chemistry Chemical Physics*
Manuscript ID	CP-ART-09-2021-004373.R1
Article Type:	Paper
Date Submitted by the Author:	24-Oct-2021
Complete List of Authors:	Varga, Zoltán; University of Minessota, Chemistry Truhlar, Donald; Department of Chemistry, University of Minnesota

Oct. 24, 2021

Potential energy surface for high-energy N + N_2 collisions

Zoltan Varga and Donald G. Truhlar*

Department of Chemistry, Chemical Theory Center, and Minnesota Supercomputing Institute, University of Minnesota, Minneapolis, Minnesota 55455-0431, USA

ABSTRACT. Potential energy surface calculations yield physical insight into the structure of intermediates and the dynamics of molecular collisions, and they are the first step toward molecular simulations that provide physical insight into energy transfer, reaction, and dissociation probabilities. The potential energy surface for high-energy collisions of N_2 with N can be used for modeling chemical dynamics and energy transfer in atmospheric shock waves. Here we present an analytic ground-state. ($^4A''$) potential energy surface for N_3 that governs electronically adiabatic collisions of $N_2(^1\Sigma_g^+)$ with N(^{4}S). The fitted surface consists of a pairwise potential based on an accurate diatomic potential energy curve plus a connected permutationally invariant polynomials (PIPs) in mixed-exponential-Gaussian bond order variables (MEGs) for the three-body part. The three-body fit is based on multireference complete active space second order perturbation theory (CASPT2) calculations. The quality of the quartet N_3 fit is comparable to that for a previous fit of the NO_2 potential. We characterize two local minima of N_3, two tight transition structures, two van der Waals geometries, and the noncollinear reaction path for the symmetric exchange reaction. The nonreactive approach of an N atom to N_2 along the perpendicular bisector is more repulsive than the collinear reproach, but plots of the force on the bond versus the potential energy at the distance of closest approach allow us to infer that vibrational energy transfer should occur much more readily in high-energy collinear collisions than in high-energy perpendicular-bisector collisions.

*Corresponding author: truhlar@umn.edu

Electronic Supplementary Information

The electronic supplementary information contains the fitting datasets for $N_3(^4A'')$, a Fortran subroutine for the MB-PIP-MEG surface (N3_4App_MB-PIP-MEG), and two examples of *OpenMolcas* input files.

ORCID numbers:
Zoltan Varga: 0000-0002-9324-798X
Donald G. Truhlar: 0000-0002-7742-7294

1. Introduction

In the electronically adiabatic approximation, collisions of ground-electronic-state $N_2(^1\Sigma_g^+)$ with ground-state $N(^4S)$ occur on a single quartet A'' potential energy surface. The objective of the present article is to provide a globally accurate analytic representation of this surface that is realistic even for high-energy collisions in shock waves. Such a surface is the first step in molecular dynamics simulations of the vibrationally and rotationally inelastic collisions and dissociative collisions of N with N_2.

Laganà and co-workers[1] considered a linear reaction path for the $N_2(^1\Sigma_g^+)$ + $N(^4S)$ exchange reaction, and represented the potential using the London–Eyring–Polanyi–Sato (LEPS) functional form. Later theoretical studies based on multireference calculations suggested that the transition state is not linear since the potential energy decreased as the linear geometry was deformed, and instead of the previously assumed linear $N_3(^4\Pi_u)$ transition state, the exchange reaction has a nonlinear minimum-energy path.[2] The stationary points of doublet and quartet N_3 were calculated by complete active space self-consistent field (CASSCF), complete active space second order perturbation theory (CASPT2), and multireference configuration interaction (MR-CI) by Zhang and coworkers.[3] Currently a symmetric double-barrier minimum-energy path is accepted for the exchange reaction; this involves a C_{2v} local minimum, $N_3(^4B_1)$, in a shallow well at the center between twin C_s transition states of ^4A symmetry. Although the LEPS PES incorrectly predicts a linear reaction path, it was used to calculate reasonably accurate thermal rate constants.[4,5,6,7] In other work, based on new geometrical information, a series of PESs (labeled L0 to L4 and L4w) were published based on a set of rotating bond order (ROBO) models.[8,9,10,6] Wang and co-workers published a global PES (WSHDSP) mainly based on single-reference coupled cluster theory, in particular UCCSD(T), and based on MRCI calculations for geometries in which all three NN bond lengths are large.[11] Later, some of the authors of the WSHDSP fit modified the PES; brief details of this new PES can be found, for example, in refs 12 and 13: all the CCSD(T) energies were discarded since it breaks down close to the dissociated geometries, and the new fit is based on 1344 averaged coupled-pair functional (ACPF) multireference calculations; also, because the original functional form did not behave properly when N_2 dissociated, the N_2 potential was replaced by a more precise one (but neither the equations nor the codes are published for the original and the modified WSHDSP fits). Although these changes were introduced, the original WSHDSP fit is still used in dynamics studies; see for

instance ref 14. The previously mentioned L4 fit[10] and L4w fit (which includes long-range interaction),[6] were designed to include the surface features of the original WSHDSP fit for the $N_2(^1\Sigma_g^+)$ + N(^{4}S) exchange reaction. The reaction probabilities of the $N_2(^1\Sigma_g^+)$ + N(^{4}S) symmetric exchange reaction calculated with the L4 and L4w PESs were also compared to the published results obtained by using the original and/or the modified WSHDSP fit.[10,6] Because the WSHDSP surface did not provide as accurate thermal rate coefficients as expected,[7] Galvão and Varandas carried out UCCSD(T) and MRCI calculations; they extrapolated those data to the complete basis set limit and fit them by a double many-body expansion (GV fit).[15]

Mankodi and co-workers[16] proposed a fit (MBP fit) for $N_3(^4A'')$ where the first singlet N_4 fit published by our group[17] was utilized. They assumed that the $N_3(^4A'')$ surface is obtained if one of the N atoms of the N_4 fit is placed far apart from the other three atoms. There are geometries where this is true, but it is not true everywhere. We will address this issue later in this article.

Although test calculations in the previous surface fitting work[11,15] showed that the single-reference UCCSD(T) method is suitable for geometries near the stationary points of the $N_3(^4A'')$ surface, most of the geometries needed for studying high-energy collisions are expected to have significant multireference character. This motivated the use of multireference methods for stretched NN distance in some of the previous fits.[11,15] Multireference methods are especially needed for geometries where all N–N distances are appreciably stretched, which are very important geometries for high-energy collisions involving vibrational energy transfer and dissociation. We also expect that multireference methods are needed for some more compressed triatomic geometries. Therefore, in the present work, we provide a global potential energy surface for $N_3(^4A'')$ based on entirely multireference CASPT2 calculations. The CASPT2 method is size extensive and size consistent; thus, CASPT2 is more suitable than MR-CISD for global potential energy surfaces, and we use CASPT2 for the present work.

We use the Born-Oppenheimer approximation so that the potential energy surface governing nuclear motion is the fixed-nuclei electronic energy including nuclear repulsion. The energies of 7174 geometries were calculated for the present work. These points map out the surface up to 2000 kcal/mol above the energy of $N_2(r_e)$ + N(^{4}S), and – because we are especially interested in a surface that is valid for high-energy collisions – about 20% of these points have energies larger than 500 kcal/mol. Two- and thee-body terms and a local patch function were

used to describe the surface. The two-body part is an accurate diatomic potential for N_2, and the many-body (MB) part (which is a three-body part in the present application) is a connected permutationally invariant polynomial (PIP) in mixed-exponential-Gaussian (MEG) bond order variables (MEGs); the resulting surface may therefore be labeled as an MB-PIP-MEG surface.

We note that the surface to be presented here, although adequate for ground-state collisions of N_2 with N, is not sufficient for termolecular collisions of N(^{4}S), which would require two doublets, four quartets (one of which is the present surface), three sextets, two octets, and one decet surface.

2. Methods

2.1. Electronic structure methods

All electronic structure calculations are performed with the 20.10 version (tag 30-ga1c588d-dirty) of the *OpenMolcas* program.[18,19]

Since the three nitrogen atoms are always in a plane, C_s symmetry was used in all calculations. Spin-orbit coupling is neglected, and only quartet basis functions with A'' symmetry are included in the wave function. The minimally augmented correlation-consistent polarized valence quadruple zeta basis set[20] (maug-cc-pVQZ) was used.

The first electronic structure step is a state-averaged CASSCF calculation,[21,22,23] in which the two lowest states were included with weights of 0.9 and 0.1. The active space consisted of 9 electrons in the nine orbitals that are nominally the 2p orbitals. This first step produces the optimized orbitals and a ground-state reference function, and in a subsequent calculation, a single-state CASPT2 calculation[24,25] was carried out for the ground state using these orbitals and this reference function. In the CASPT2 calculations, the 1s and 2s orbitals were excluded from the electron excitations, and an imaginary shift[26] of 0.1 a.u. was applied. With these options the calculated dissociation energy of N_2 is 228.3 kcal/mol. This is very close to the experimental value (228.4 kcal/mol); therefore, a scaled external correlation[27] treatment (as used in several of our previous papers) was not needed in this case.

2.2. Selection of geometries for fitting

A significant portion (5,281 points) of the geometries calculated for the surface fitting were based on uniform grids in Jacobi coordinates. The Jacobi coordinates consist of the distance (R)

between two atoms, the distance (d) of a third atom from the center of the first pair, and the angle (γ) defined by the third atom, the geometric center of the diatom, and one of the atoms in the diatom. In the basic grid, the values of γ were set in the range 90 to 180 deg with a 10 deg increment; the values of d were set in the range 0.7 to 2.5 Å with a 0.1 Å increment, plus 2.7, 3.0, 3.4, 4.0, and 5.0 Å; and the values of R were set in the range 0.7 to 2.1 Å with a 0.1 Å increment plus 2.3, 2.5, 2.7, 3.0, 3.4, 4.0, and 5.0 Å. This basic grid was extended with additional points for γ = 150, 160, 170, and 180 deg; for these γ values, the d values were set to 2.6, 2.8, 2.9, 3.2, 3.6, 3.8, 4.2, 4.4, 4.7 Å; and the R values were set to 2.0–3.2 Å with a 0.1 Å increment plus 3.4, 3.6, 3.8, 4.0, 4.3, 4.6, 4.9, and 5.2 Å. For both the basic and the extended grids, any geometry at which any of the internuclear distances is shorter than 0.7 Å was left out.

Multi-dimensional scans were then carried out to find regions with poor data coverage, especially for packed N_3 geometries. The three NN internuclear distances (r_1, r_2, r_3) for each geometry point (denoted as i) of the fitting data set were re-arranged in ascending order ($r_{A,i} \leq r_{B,i} \leq r_{C,i}$). In the first multi-dimensional scan, the NN distances (denoted as $r_{a,j}$, $r_{b,j}$, $r_{c,j}$, where j labels a geometry of the scan) were varied between 0.7 and 2.0 Å with a 0.1 Å increment, where $r_{a,j} \leq r_{b,j} \leq r_{c,j}$ and only the valid triangle structures were considered. The distance between each geometry i in the dataset and each geometry j in the multi-dimensional scan was calculated by

$$s_{i,j} = \sqrt{(r_{A,i} - r_{a,j})^2 + (r_{B,i} - r_{b,j})^2 + (r_{C,i} - r_{c,j})^2} \quad (1)$$

and the minimum of value of $s_{i,j}$ was calculated for each j:

$$S_j = \min_i(s_{i,j}) \quad (2)$$

If S_j was larger than a threshold value of 0.15 Å, point j was considered to be in a vacant geometry region and collected in a list. The energies at the geometries in the list were calculated by CASPT2, and they were added to the data set. In a second multi-dimensional scan, the range of the NN distances ($r_{a,j}$, $r_{b,j}$, $r_{c,j}$) was 0.7-4.0 Å with a 0.1 Å increment; in this scan, the threshold value for considering a point to be in a vacant geometry region is increased to 0.2 Å. Only a subset of the energies in this second list were calculated by CASPT2 since many of them are dissociated or almost dissociated (that is, they correspond to three largely separated N atoms) and those kinds of geometries are reasonably described by the diatomic potential term of the fit (see section 2.3.1). Altogether 162 points were added to the data set from these two multi-dimensional scans.

By using a preliminary fit of the N_3 surface, some N_2 + N trajectory calculations[28] were carried out. The initial conditions of 500 trajectory runs were picked to generate geometry points with high energies; in particular the relative translational energy was set to 70 eV; the boundaries of the impact parameter are 0 and 1.6 Å; the vibrational and rotational quantum numbers of the diatomic molecule are 15 and 29, respectively; and the initial atom–diatom separation is 4 Å. The trajectories were terminated when any of the internuclear distances becomes longer than 4.2 Å. The Bulirsch-Stoer integrator with adaptive step size was used, and at each time step the geometry and its energy was saved into a list. From this list, all the points with fitted energy higher than 450 kcal/mol were calculated by CASPT2, and the points with energy lower than 2000 kcal/mol were added to the fitting data set (265 points). (The three atoms are usually close to one another for these high-energy points.) Additionally, the first 250 points of this list with energy between 450 and 230 kcal/mol were also calculated by CASPT2 and added to the fitting data set. These trajectory runs were carried out with the ANT program.[29]

The stationary structures of N_3 ($^4A''$) surface, which are known from the literature, were optimized by CASPT2 and additional geometries in the vicinity of these stationary structures were added to the data set. This includes the regions near the $^4B_1$ minimum (141 points), the $^4\Pi$ transition state (112 points), a $^4A''$ transition state (126 points), and a quartet D_{3h} minimum (574 points). The relatively large number of points around the D_{3h} minimum is needed for mapping the surface for a patch function described in section 2.3.3.

An additional 263 geometries in the van der Waals region of N_2 + N were calculated by CASPT2 and added to the fitting data set.

Altogether the above approaches yield the energies of 7,174 geometries with energies up to 2000 kcal/mol.

2.3. Functional from of the potential energy surface fitting

The potential energy surface of the $N_3(^4A'')$ state is expressed as a global function V_G modified with a patch function V_{PF}:

$$V = V_G(r_1,r_2,r_3) + V_{PF}(r_1,r_2,r_3) \quad (3)$$

where (as above) r_1, r_2, and r_3 denote the three NN distances. The details of the local patch function which is intended to restore the local minimum nature of a stationary structure previously studied in ref 15, are explained in section 2.3.3.

The global function is a connected many-body, permutationally-invariant-polynomial, mixed-exponential-Gaussian[30,31] (MB-PIP-MEG) fit, and it uses the following expansion:

$$V_{\mathrm{G}} = V_0 + \sum_{i=1}^{3} V_{\mathrm{PA}}(r_i) + V_{\mathrm{MB}}(r_1,r_2,r_3) \quad (4)$$

where V_0 is a constant; V_{PA} is the $N_2(^1\Sigma_g^+)$ pairwise potential, which is explained in section 2.3.1, and V_{MB} is the many-body term, which is a three-body term in this current work and is explained in section 2.3.2. The zero of energy for the present surface corresponds to equilibrium $N_2(^1\Sigma_g^+)$ infinitely separated from N(^{4}S); to obtain this zero of energy, V_0 is set equal to the dissociation energy of N_2, i.e., 228.4 kcal/mol.

2.3.1. Diatomic potential

In our most recent work on N_4,[31] we published a new pairwise potential for $N_2(\Sigma_g^+)$, which was slightly modified further in the present work. The dissociation energy of the pairwise potential in the N_4 work is 228.7 kcal/mol as in the previous N_4 fits in our group.[17,32] This dissociation energy is slightly larger than the experimental dissociation energy (228.4 kcal/mol) used in other surfaces for N_xO_y systems published by our group. For individual studies of the N_xO_y systems, such a small difference in the pairwise potentials do not lead to significantly different results. However, for simulating hot air in a shock wave, it is preferable to have set of surfaces for which all the N_2 and O_2 diatomic potentials are consistent (i.e., independent of which surface is being used for a given collision). We have therefore created a consistent set of surfaces that employ the same N_2 and O_2 diatomic potentials. For this purpose, the diatomic potential of the MB-PIP-MEG fit of the N_4 PES was updated with the new diatomic potential, it is called N4_1A_MB-PIP-MEG3, and it can be downloaded from the POTLIB library.[33,34] The N_2 potential used for the present N_3 potential conforms to that consistent set of diatomic potentials.

In particular, the functional form of the N_2 potential includes a short-range term (V_{SR}) and a damped-dispersion term ($V_{\mathrm{D3(BJ)}}$):

$$V_{\mathrm{PA}}(r_i) = V_{\mathrm{SR}}(r_i) + V_{\mathrm{D3(BJ)}}(r_i) \quad (5)$$

The damped-dispersion term is based on Grimme's D3 dispersion parameters with the Becke-Johnson damping (BJ) damping function:[35,36]

$$V_{\mathrm{D3(BJ)}}(r_i) = \sum_{n=6,8} {}^{s_n C_n} \Big/ \left[r_i^n + \left(a_1 \sqrt{C_6 / C_8} + a_2 \right)^n \right] \quad (6)$$

where the parameters s_6 and s_8 are 1.0 and 2.0, respectively. The parameters a_1 and a_2 were set to 0.5299 bohr^2 (corresponds to 0.14839 Å^2) and 2.2 bohr (corresponds to 1.16419 Å), respectively, based on Ref. 37. The C_6 constant is 19.7 in atomic units (corresponds to 271.45 kcal Å^6/mol). The C_8 parameter is calculated from C_6 by the formula used in Refs. 35 and 36. This yields C_8 equals 434.598 in atomic units.

The short-range term of the diatomic potential, is a generalized Morse fit to the difference of the original diatomic potential (see the supplementary material of Ref. 17) and the damped-dispersion term:

$$V_{\mathrm{SR}}(r_i) = D_{\mathrm{SR}}[1 - \exp(-f(r_i - r_e))]^2 - D_{\mathrm{SR}} \tag{7}$$

where D_{SR} is 224.9157 kcal/mol (obtained by subtracting the value of the damped-dispersion potential at the equilibrium distance from the dissociation energy of $N_2(\Sigma_g^+)$, r_e is 1.098 Å, and f is expressed as

$$f = \sum_{k=0}^{6} a_k \left(\frac{r_i^4 - r_e^4}{r_i^4 + r_e^4}\right)^k \tag{8}$$

where a_0 = 2.7599278840949 Å^{-1}, a_1 = 0.2318898277373 Å^{-1}, a_2 = 0.1908422945648 Å^{-1}, a_3 = -0.2727504034613 Å^{-1}, a_4 = -0.5345112219335 Å^{-1}, a_5 = 1.0857331617073 Å^{-1}, and a_6 = 1.6339897930305 Å^{-1}.

2.3.2. Many-body potential

The many-body term of the potential energy is expressed as

$$V_{\mathrm{MB}}(r_1,r_2,r_3) = \sum_{\substack{\text{connected,}\\ n_1+n_2+n_3=2}}^{l} D_{n_1 n_2 n_3} S\left[X_1^{n_1} X_2^{n_2} X_3^{n_3}\right] \tag{9}$$

where $S[\ldots]$ is a permutationally invariant polynomial basis function obtained by symmetrization of a primitive monomial basis functions, as originally developed by Xie and Bowman.[38,39] The restriction to connected terms was introduced in Ref. 17. A tenth order (l = 10) many-body functions was used for the $N_3(^4A'')$ system, which contains 56 $D_{n_1 n_2 n_3}$ fitting coefficients. For the bond order variables, X_i, mixed exponential-Gaussian functions[32] were used:

$$X_i = \exp\left[-(r_i - r_e)/a - (r_i - r_e)^2/b\right] \tag{10}$$

where the nonlinear parameters a, b, and r_e are 1.28 Å, 2.10 Å^2, and 1.098 Å, respectively.

The four-body frame of a general A_4 system was applied for making the fit of the $N_3(^4A'')$ system. This treatment is the same as the fits of other three-body systems (N_2O, O_3, NO_2) carried

out by our group.[30,40,41] Considering this general scheme as an N_4 system, one of the nitrogen atoms was placed far apart from the other three nitrogen atoms.

To carry out of the fit of the many-body term, the following error function is minimized:

$$F = \sum_{j=1}^{n} W_j \left(V_j^{0,\mathrm{PA}} - V_j + \sum_{k=1}^{m} d_k s_{jk} \right)^2 \quad (11)$$

ith respect to the linear coefficients d_k, where m and n are the number of basis functions and the number of fitted data points, respectively, $V_j^{0,\mathrm{PA}}$ is the sum of the constant and pairwise terms at geometry point j, V_j is the energy of geometry point j, d_k is the k-th $D_{n_1 n_2 n_3}$ coefficient, s_{jk} is the k-th basis function $S\left[X_1^{n_1} X_2^{n_2} X_3^{n_3}\right]$ evaluated at geometry point j, and W_j is a weighting function used to avoid too much emphasis on the high-energy data points:

$$W_j = \begin{cases} 1 & \text{for } V_j \le (E_c + E_{sh}) \\ \left[(E_c + E_{sh}) / V_j \right]^p & \text{for } V_j > (E_c + E_{sh}) \end{cases} \quad (12)$$

where E_c is a parameter of the fitting process that reduces the weights of very-high-energy data points. The parameter E_{sh} is arbitrarily set equal to 228.4 kcal/mol, which is dissociation energy of $N_2(\Sigma_g^+)$ as well as the energy difference between the reference energies of the four- and three-body frames. We chose E_c and the power p to be 100.0 kcal/mol and 1.5, respectively.

The potential energy surface of the $N_3(^4A'')$ system was fitted by a modified version of our *PIPFit* program.[42]

2.3.3. A local patch function

The quartet A'' energy surface of N_3 has a local minimum with an equilateral triangle (D_{3h}) structure. This minimum is shown in Fig. 1, where two of the NN distances are varied together ($r_1 = r_2$), and the angle between these two NN distances (α_3) is also varied. The D_{3h} structure is located at the minimum energy point of the central well in this figure, where the bond angle is 60 deg. The topography near the local minimum is like that of a volcanic crater.[15,43] The ground-state energy increases as the structure is distorted, and we see ridges for bond angles ~47 deg and ~70 deg, due to a diabatic crossing with another electronic state. Preliminary fits of the surface showed that the fitting form is not flexible enough to properly fit this region of the surface. The crossing seam structure was completely missing in these fits, and the (D_{3h}) high-energy local minimum structure was turned into a hilltop, i.e., a second-order transition state. To obtain the expected surface shape in this region of the surface, we introduced a local patch

function. In a manual iterative process, the energy of the test patch function was added to the (relative) CASPT2 energy at each geometry (due to the local nature of the patch function, this does not change the CASPT2 energy for most of the geometries). This turns local minimum into a hilltop for the fitting, but it is pushed up to higher energies. Then, after this, the energy of the test patch function was subtracted from the energy of the fit at each geometry (again, due to the local nature of the patch function, this does not change the energy of the fit for most of the geometries). The shape of the surface was visually checked, and the parameters of the patch function were adjusted accordingly to get the desired surface shape.

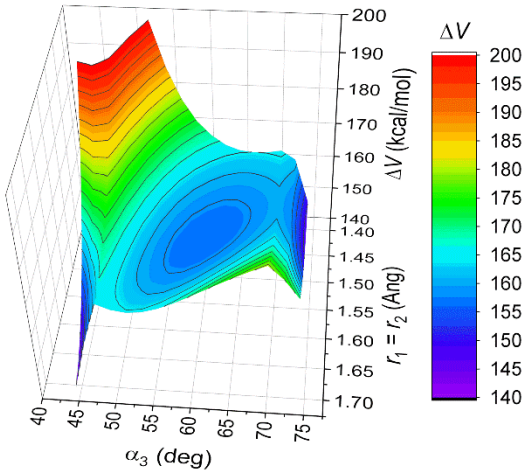

Figure 1. A surface cut of the well of the D_{3h} local minimum calculated by CASPT2.

The patch function used for the above procedure is complicated because preliminary calculations showed that a simple path function did not suffice. In the finally adopted patch functional, the two NN bond lengths and the bond angle between those two bonds are used, and to enforce permutational invariance, all three combinations are considered.

$$V_{\mathrm{PF}} = -b_0\{G_1 + G_2 + G_3\} \tag{14}$$

where

$$G_1 = \exp\left[-(b_1(r_1 - r_{\mathrm{f}}))^2 - (b_1(r_2 - r_{\mathrm{f}}))^2 - (b_2(\cos\alpha_3 - \cos\alpha_{\mathrm{f}}))^2\right] \tag{15a}$$

$$G_2 = \exp\left[-(b_1(r_1 - r_{\mathrm{f}}))^2 - (b_1(r_3 - r_{\mathrm{f}}))^2 - (b_2(\cos\alpha_2 - \cos\alpha_{\mathrm{f}}))^2\right] \tag{15b}$$

$$G_3 = \exp\left[-(b_1(r_2 - r_{\mathrm{f}}))^2 - (b_1(r_3 - r_{\mathrm{f}}))^2 - (b_2(\cos\alpha_1 - \cos\alpha_{\mathrm{f}}))^2\right] \tag{15c}$$

where b_0, b_1, and b_2 are adjustable parameters, and r_{f} and α_{f} are the bond length and bond angle of the focus point, respectively. The final values of the parameters are collected in Table 1.

Table 1. Parameters of the patch function

parameter	value, unit
r_f	1.532 Å
α_f	1.0472 rad (60°)
b_0	17.0 kcal/mol
b_1	3.4 Å^{-1}
b_2	6.8 rad^{-1}

3. Results and discussion

3.1. Error statistics

The root-mean-square errors (RMSEs) and mean unsigned errors (MUEs) of the MB-PIP-MEG fit with respect to the data set energies are collected in Table 2, where they are sorted into five energy ranges. The table also includes a comparison to the GV fit of $N_3(^4A'')$ by Galvão and Varandas.[15] Column 1 of the table is the energy range under consideration. Columns 2 and 3 are respectively the number of GV data points in that range and the root-mean-square error (RMSE) of their fit to their data. Column 4 contains the number our data points in each energy interval. In the lower two energy ranges, 0–100 and 100–250 kcal/mol, the GV fitting data set is based on enough points to get a good fit, and the RMSEs of the GV fit to the GV data are very good in these energy ranges. However, in the upper three energy ranges 250–500, 500-1000, and above 1000 kcal/mol we have about 8, 17, and 6 times more points, respectively, than those in the GV fitting data set. Columns 5 and 6 present the RMSEs of the GV fit and of our fit to our data set. We see that, although the GV fit is in a good agreement with their data, it agrees less well with our more extensive dataset covering a more diverse set of geometries such that the RMSEs of their fit are significantly higher with our data set than with theirs. This comparison shows the difficulty of creating a global potential energy surface over a very wide range of energies; the errors are larger than fits on other systems in the literature where the goal was higher accuracy in a more localized region of geometries with mainly low energies.

The final column of Table 2 gives the mean unsigned error (MUE, which a more robust[44,45] error indicator than RMSE). The overall MUE of the current 10-th order MB-PIP-MEG fit for

$N_3(^4A'')$ is very comparable with the MUE (2.4 kcal/mol) of 12-th order MB-PIP-MEG fit for quartet NO_2.[30]

Table 2. Root-mean-square errors (RMSEs in kcal/mol) and mean unsigned errors (MUEs in kcal/mol) of the $N_3(^4A'')$ fit for various energy ranges

Energy range (kcal/mol)	Number of points in GV dataset[a]	RMSE of GV fit[a] to GV dataset	Number of points in our dataset	RMSE of GV fit[a] to our dataset	RMSE of our fit to our dataset	MUE of our fit to our dataset
$0 \le \Delta V < 100$	1073	0.7	1932	6.6	1.5	1.0
$100 \le \Delta V < 250$	370	1.4	3798	9.4	3.7	2.0
$250 \le \Delta V < 500$	85	1.5	692	12.9	7.4	5.2
$500 \le \Delta V < 1000$	36	1.3	616	23.1	8.9	6.8
$1000 \le \Delta V < 2000$	21	1.8	136	87.4	13.9	10.0
all data	1585	1.0	7174	16.4	4.9	2.6

[a]See Ref. 15 for the details of the Galvão and Varandas (GV) fit and data set.

3.2. Stationary points

The stationary structures of the $N_3(^4A'')$ fit were optimized by the *Polyrate* program,[46] and we also optimized the stationary structures by CASPT2. The resulting geometries and energies as well as those of previous works are collected in Table 3. In general, the CASPT2 calculations used in this work predict slightly higher relative energies for the tight N_3 stationary points than those used in the fitting of the WSHDSP,[11] L4,[10] and GV[15] surfaces, which were mainly obtained by single-reference CCSD(T). This the relative values of our fit are also higher.

The M diagnostic[47] allows one to infer whether the electronic structure is strongly correlated, i.e., has high multireference character. The M diagnostics were therefore computed for the stationary structures, and they are included in Table 3. For the tight N_3 structures, the M diagnostic shows moderate (0.05 – 0.10) or large (≥ 0.10) multireference character. The van der Waals complexes and the separated atom–diatom structure also have moderate multireference character. Systems with moderate or large multireference character are best treated with multireference methods,[47] as is done here.

In addition to the asymptotic $N_2(^1\Sigma_g^+)$ + N(^{4}S) structure, there are two N_3 local minima on the ground quartet surface, namely a C_{2v} bent structure with $^4B_1$ symmetry that lies 53.1 kcal/mol

higher than the asymptotic stationary point and a much higher D_{3h} structure with symmetry $^4A_2''$ at 154.2 kcal/mol. The latter is the structure that required the patch function mentioned in section 2.3.3.

Table 3 has two transition structures. Reaction path calculations with C_s symmetry show that the $^4A''$ transition structure connects on one side to a $N_2(^1\Sigma_g^+)\cdots N(^4S)$ van der Waals well and on the other side to the $N_3(^4B_1)$ stationary point. Therefore, the reaction path for the symmetric exchange reaction of the fitted surface has twin saddle points flanking this local minimum. The reaction path was calculated by *Polyrate* as the minimum energy path in isoinertial coordinates[48] scaled to 1 amu. This was done by following the path of steepest descent from each of the twin saddle points and joining these paths where they meet at the $N_3(^4B_1$ local minimum. The potential energy profile along the resulting merged path is shown in Fig. 2; at selected points along the path, the geometries (two bond lengths and a bond angle) are also shown. These geometries along the path show that the bond angle becomes smaller as the N atom separates from N_2, and the path tends toward a perpendicular-bisector (i.e., T-shaped) atom–diatom van der Waals well.

We also characterized the reaction path that passes through the $N_3(^4\Pi_u)$ transition structure with $D_{\infty h}$ symmetry. This path also has C_s symmetry, and it shows that the $N_3(^4\Pi_u)$ transition structure is the inversion structure between two $N_3(^4B_1)$ stationary points.

In the fitted surface, the van der Waals interaction is stronger than data to which it was fit; the fitted surface, like the CASPT2 calculations, has a minimum with a T-shaped geometry. This corresponds to the perpendicular atom-diatom arrangement of the exchange reaction path calculation shown in Fig. 2. The interaction energy is slightly weaker in the close-to-collinear arrangement, which is a transition structure.

Table 3. Stationary structures on the $N_3(^4A'')$ surface

	method	ΔV, kcal/mol	r_1, Å	r_2, Å	α_3, deg
$N_2(^1\Sigma_g^+)$ + N(^{4}S)	this fit	0.0	1.098	-	-
M = 0.06	CASPT2/maug-cc-pVQZ	0.0	1.096	-	-
	GV fit[a]	0.0	1.098	-	-
	Tight minima				
$N_3(^4B_1)$	this fit	53.1	1.271	1.271	115.6

$M = 0.10$	CASPT2/maug-cc-pVQZ	54.4	1.265	1.265	117.2
	GV fit[a]	42.9	1.261	1.261	119.1
	CCSD(T)/CBS[a]	42.9	1.259	1.259	119
	WSHDSP fit[b]	43.7	1.270	1.270	120
	CCSD(T)/aug-cc-pVTZ[b]	44.7	1.265	1.265	119
	L4 fit[c]	44.5	1.270	1.270	119
	MBP fit[d]	44.7	1.262	1.262	120
	CASPT2(g4)/aug-cc-pVQZ[e]	36.9	1.266	1.266	119
	MR-CISD+Q/aug-cc-pVTZ[e]	43.9	1.271	1.271	118.5
$N_3(^4A_2'')$	this fit	154.2	1.540	1.540	60.0
$M = 0.12$	CASPT2/maug-cc-pVQZ	156.1	1.522	1.522	60.0
	GV fit[a]	146.6	1.561	1.561	60.0
Tight transition structures					
$N_3(^4A'')$	this fit	56.5	1.181	1.481	116.7
$M = 0.08$	CASPT2/maug-cc-pVQZ	56.5	1.175	1.480	115.0
	GV fit[a]	45.9	1.163	1.498	116.4
	CCSD(T)/CBS[a]	45.9	1.164	1.508	117
	WSHDSP fit[b]	47.2	1.180	1.482	119
	CCSD(T)/aug-cc-pVTZ[b]	47.1	1.175	1.503	117
	L4 fit[c]	47.4	1.185	1.466	117
	MBP fit[d]	47.1	1.180	1.480	119
	CASPT2(g4)/aug-cc-pVQZ[e]	41.2	1.169	1.176	117.2
	MR-CISD+Q/aug-cc-pVTZ[e]	46.4	1.176	1.505	117.2
$N_3(^4\Pi_u)$	this fit	112.4	1.246	1.246	180.0
$M = 0.12$	CASPT2/maug-cc-pVQZ	112.3	1.242	1.242	180.0
	GV fit[a]	91.8	1.264	1.264	180.0
	CASPT2(g4)/aug-cc-pVQZ[e]	98.9	1.271	1.271	180.0
	MR-CISD+Q/aug-cc-pVTZ[e]	106.3	1.273	1.273	180.0
van der Waals stationary points					
$N_2(\Sigma_g^+)\cdots N$ [MIN]	this fit	-0.09	1.098	4.182	82.3
$M = 0.06$	CASPT2/maug-cc-pVQZ	-0.04	1.096	4.109	82.4
	GV fit[a]	-0.23	1.098	3.548	81.2
$N_2(\Sigma_g^+)\cdots N$ [TS]	this fit	-0.06	1.098	4.145	180.0

M = 0.06	CASPT2/maug-cc-pVQZ	-0.02	1.096	4.039	180.0
	GV fit[a]	-0.20	1.098	3.530	180.0

[a] Ref 15, the structures of the GV fit were optimized by *Polyrate* program.

[b] Ref 11.

[c] Ref 10.

[d] Ref 16.

[e] Ref 3.

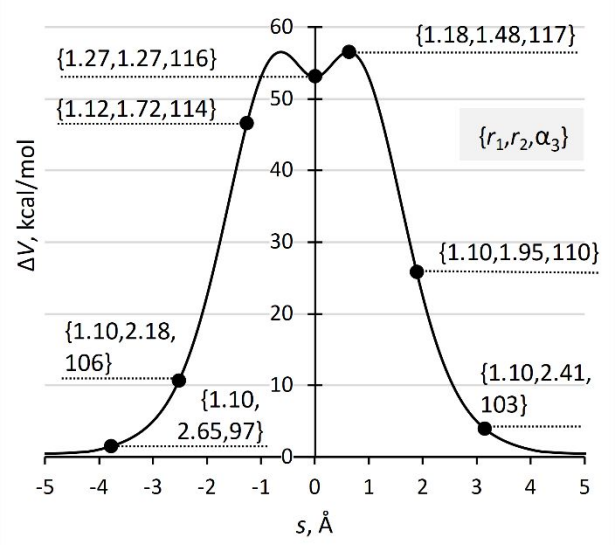

Figure 2. Minimum energy path of $N_2(^1\Sigma_g^+)$ + N(^{4}S) exchange reaction. The origin of the reaction coordinate s (which measures arc length along the path in isoinertial coordinates) is chosen at the $N_3(^4B_1)$ stationary point, although the actual calculation of the path involves following the paths of steepest descent down from each of the twin saddle points. At selected points along the path, the geometries are also shown in curly brackets. The bond lengths (r_1 and r_2) are in Å, and the bond angle (α_3) is in degrees.

The harmonic vibrational frequencies of stationary structures of the $N_3(^4A'')$ fit are collected in Table 4.

Table 4. Harmonic vibrational frequencies of stationary structures on the $N_3(^4A'')$ fitted surface

Structure	Frequencies, cm^{-1}
$N_2(^1\Sigma_g^+)$ + N(^{4}S)	2403
$N_3(^4B_1)$	1289, 854, 667

$N_3(^4A_2'')$	1476, 1174, 74
$N_3(^4A'')$	1589, 662, 742*i*
$N_3(^4\Pi_u)$	1015, 401, 876*i*, 876*i*
$N_2(\Sigma_g^+)\cdots N$ [MIN]	2403, 22, 15
$N_2(\Sigma_g^+)\cdots N$ [TS]	2403, 19, 6*i*

The MBP fit of N_3 presented by Mankodi and coworkers[16] was obtained by refitting the surface of our first singlet N_4 PES[17] for geometries where one of the N atoms is very far from the other three N atoms and they use this surface as if were an $N_3(^4A'')$ surface. Unfortunately, this is not a valid procedure. In the adiabatic ground-state calculations of the four-body N_4 system, the overall spin state is a singlet, but the subsystem spin states are not controlled; for example, one could have an N_3 doublet coupled to an N atom doublet to make an overall singlet. For geometries of the type N_2 + 2N, one does expect that the lowest-energy N_4 singlet state corresponds to either N_3 subsystem being a quartet. But the excitation energy from N(^{4}S) to N(^{2}D) is only 55.0 kcal/mol[49] (when spin-orbit coupling is not considered); therefore, for any geometry where the N_3(doublet) sub-system is lower in energy by 55.0 kcal/mol than the energy of the N_3(quartet) sub-system, the N_3(doublet) + N(^{2}D) will be the ground electronic state. To illustrate this issue, we consider geometries near the C_{2v} symmetry $N_3(^2B_1)$ local minimum. For the cut shown in Fig. 3, one of the NN distances (r_3) is fixed at 1.2 Å, and the other two NN distances are equal ($r_1 = r_2$) and varied between 1 to 2.5 Å. The plotted energies are the MBP fit CASPT2 calculations of the $N_3(^4A'')$ and $N_3(^2A'')$ states (except the spin state, the details of the doublet calculations are the same as we used for the quartet CASPT2 calculations). Note that the doublet curve is shifted by 55.0 kcal/mol, i.e., the N(^{4}S) to N(^{2}D) transition energy. The plot clearly shows that the MBP fit agrees better with the quartet energies at longer bond lengths, and it agrees better with the doublet energies at shorter bond lengths, i.e., with the well of the $N_3(^2B_1)$ structure. This is what is expected from the discussion above because this corresponds to the correct lowest-energy singlet of the N_4 system with one N atom far away. Therefore, the MBP surface is invalid.

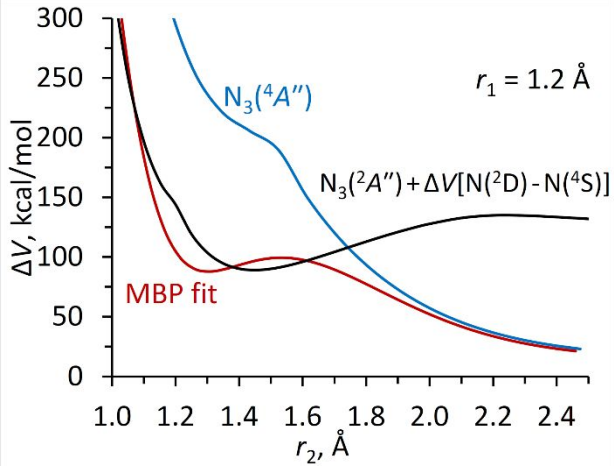

Figure 3. Comparison of the energies of $N_3(^4A'')$ and $N_3(^2A'')$ states calculated by CASPT2 and MBP fit. The energies of the $N_3(^2A'')$ are shifted by the transition energy (55 kcal/mol) between $N(^4S)$ and $N(^2D)$.

3.3. Illustrative cuts

Figures 4 and 5 show illustrative one-dimensional cuts (for a collinear and a perpendicular collision, respectively) through the fitted N_3 surface developed in this article. In these plots, three curves are shown, one (r_1) of the N-N distances is fixed at r_e of N_2 molecule (blue), and – to show the effect of vibrational excitation – the other two have r_e stretched by 0.3 Å (red) and 0.6 Å (black). To represent the collision coordinate, another NN distance (r_2) is scanned from 5 Å to about 0.7 Å.

As was discussed in Ref. 2, the $N_2(^1\Sigma_g^+)$ + $N(^4S)$ collision partners have a Σ ground state for a collinear collision, but the collinear transition state of N_3 is a $^4\Pi_u$ state. Figure 4 shows how the Σ and Π states cross. For $r_1 = r_e$, this is only a shoulder, which temporarily decreases the steepness of the repulsive curve as r_2 becomes smaller. For r_e + 0.3 Å, the Π state starts forming a well inside the crossing, and for r_e + 0.6 Å, where the Σ state already has a high energy for larger r_2 values, the crossing is only a small bump and the well of the Π state is a significant feature.

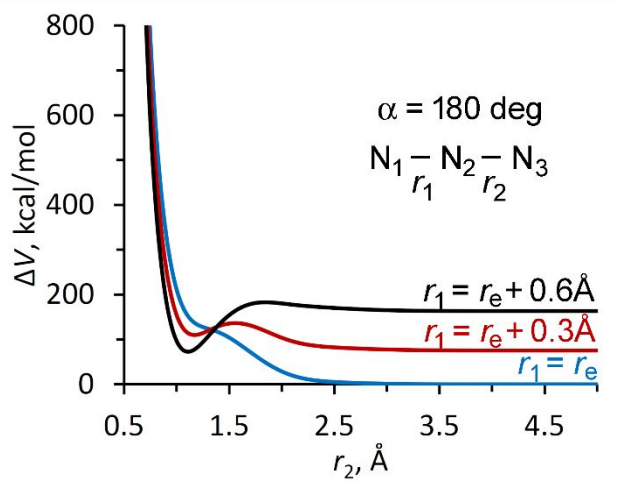

Figure 4. Potential energy for collinear approach of N to N_2. One curve is for N_2 at its equilibrium internuclear distance (1.098 Å), and the other two curves are for N_2 stretched by 0.3 Å and 0.6 Å.

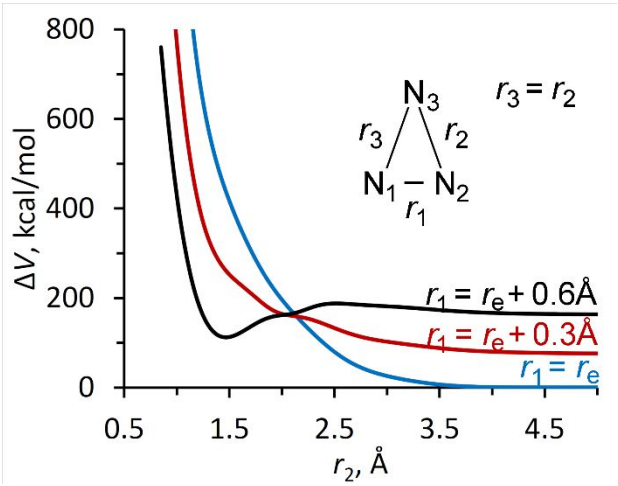

Figure 5. Potential energy for approach of N along the perpendicular bisector of N_2. One curve is for N_2 at its equilibrium internuclear distance (1.098 Å), and the other two curves are for N_2 stretched by 0.3 Å and 0.6 Å.

The approach of an atom along the perpendicular bisector (Fig. 5) is more repulsive than the collinear reproach (Fig. 4). The cuts in the stretched cases run close to the N_3 $^4A_2''$ D_{3h} structure, and the multiple state crossings in that region were already shown in Fig. 1. The surface cuts of the stretched cases show some ruggedness because of locally avoided surface crossings. The geometries in this figure provide good examples of cases that need a multireference treatment. To gain physical insight into the forces responsible for vibrational

energy transfer in the collinear and perpendicular collisions, we made additional kinds of plots for the fitted surface that are presented in Figs. 6 and 7.

For Fig. 6, we used *Polyrate* to optimize the bond length ($R = r_1$) of the diatomic molecule for a series of fixed d distances (recall that d is the distance of a third atom from the center of the diatomic molecule); the orientation angle was also fixed, corresponding first to collinear approach (panels a and b) and then to perpendicular-bisector approach (panels c and d). These optimized bond lengths R are shown in Fig. 6, first as functions of the d value at each point on the path (panels a and c) and then as functions of the potential energy at each point on the path (panels b and d). Although the distance variable (d) is a more straightforward abscissa, the physical implications of panels a and c are obscured by the fact that a collision with a given relative translational energy will reach a different d value in the perpendicular-bisector case than in the collinear case. Replotting versus the potential energy allows us to compare the optimum vibrational extension on the two paths near the translational turning points for a given translational energy, which is more relevant physically. For collinear arrangement (Figs. 6a and 6b) as the atom approaches the diatomic molecule, moving right to left in the plots, the equilibrium bond length of the diatomic molecule first increases (by 0.004 Å around d = 2.75 Å with the relative potential energy below 10 kcal/mol) due to van der Waals forces, then decreases (by 0.003 Å around d = 2.45 Å with the relative potential energy in the range 10–70 kcal/mol) due to pairwise repulsion, and then increases rapidly due to incipient bond equalization in the exchange reaction. For the perpendicular arrangement (Figs. 6c and 6d) we see a different pattern. As the third atom approaches, R first decreases and around d = 2.1 Å, the decrease of R is about 0.008 Å with respect to the equilibrium bond length of the free diatomic molecule. For shorter d values, R is rapidly increasing. Comparing the optimal R distances in Figs. 6b and 6d shows that at any given potential energy, R is slightly shorter for the T-shaped path than the I-shaped one. The optimal R distances are the closest to each other at ~75 kcal/mol (with d of 2.2 Å for the I-shaped approach and 1.75 Å for the T- one). If one converts the Jacobi coordinates to internuclear distances, then the collinear d of 2.2 Å corresponds to a nearest-neighbor distance of 1.68 Å, and the d of 1.75 Å for the perpendicular case corresponds to a nearest-neighbor distance of 1.83 Å.

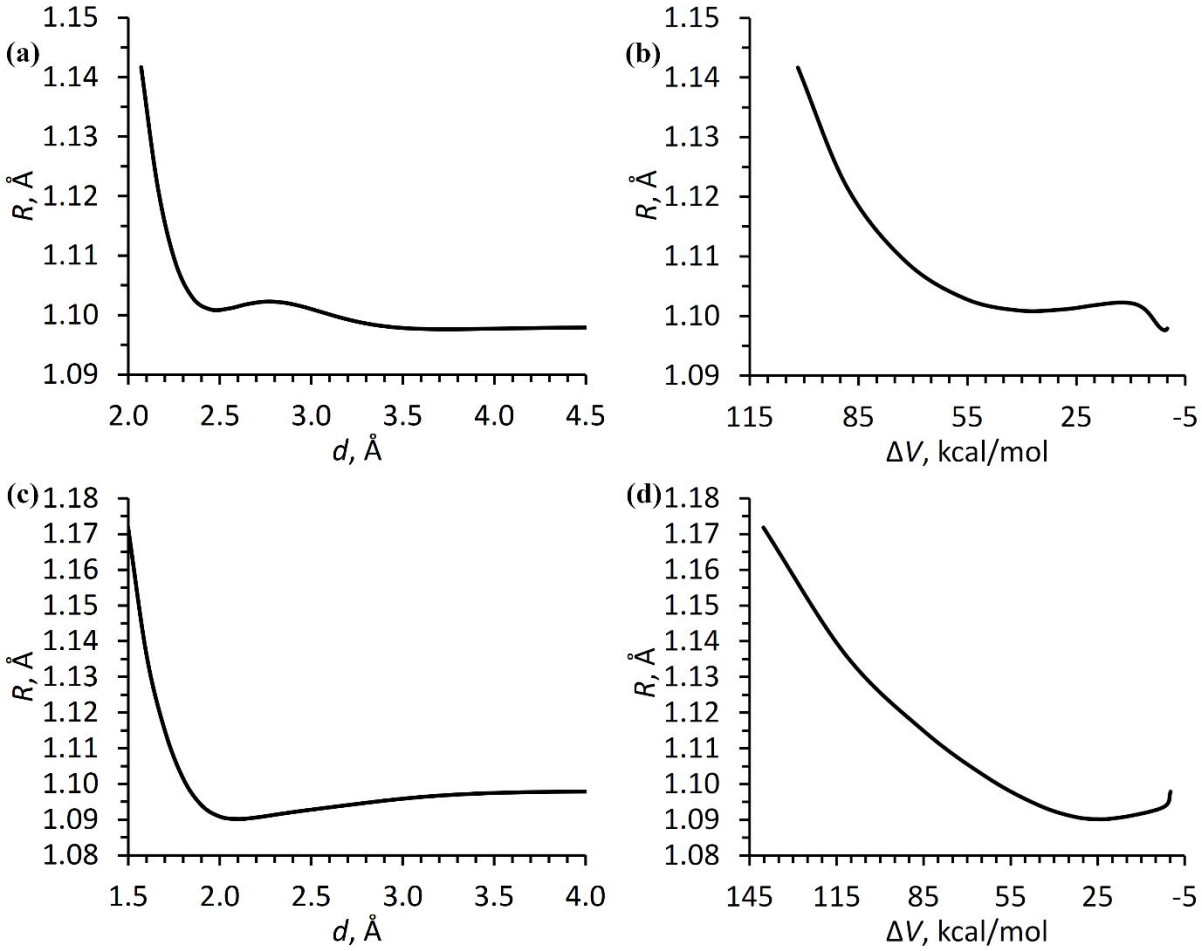
(a)
1.15
1.14
1.13
1.12
1.11
1.10
1.09
R, Å
2.0
2.5
3.0
3.5
4.0
4.5
d, Å
(b)
1.15
1.14
1.13
1.12
1.11
1.10
1.09
R, Å
115
85
55
25
-5
ΔV, kcal/mol
(c)
1.18
1.17
1.16
1.15
1.14
1.13
1.12
1.11
1.10
1.09
1.08
R, Å
1.5
2.0
2.5
3.0
3.5
4.0
d, Å
(d)
1.18
1.17
1.16
1.15
1.14
1.13
1.12
1.11
1.10
1.09
1.08
R, Å
145
115
85
55
25
-5
ΔV, kcal/mol

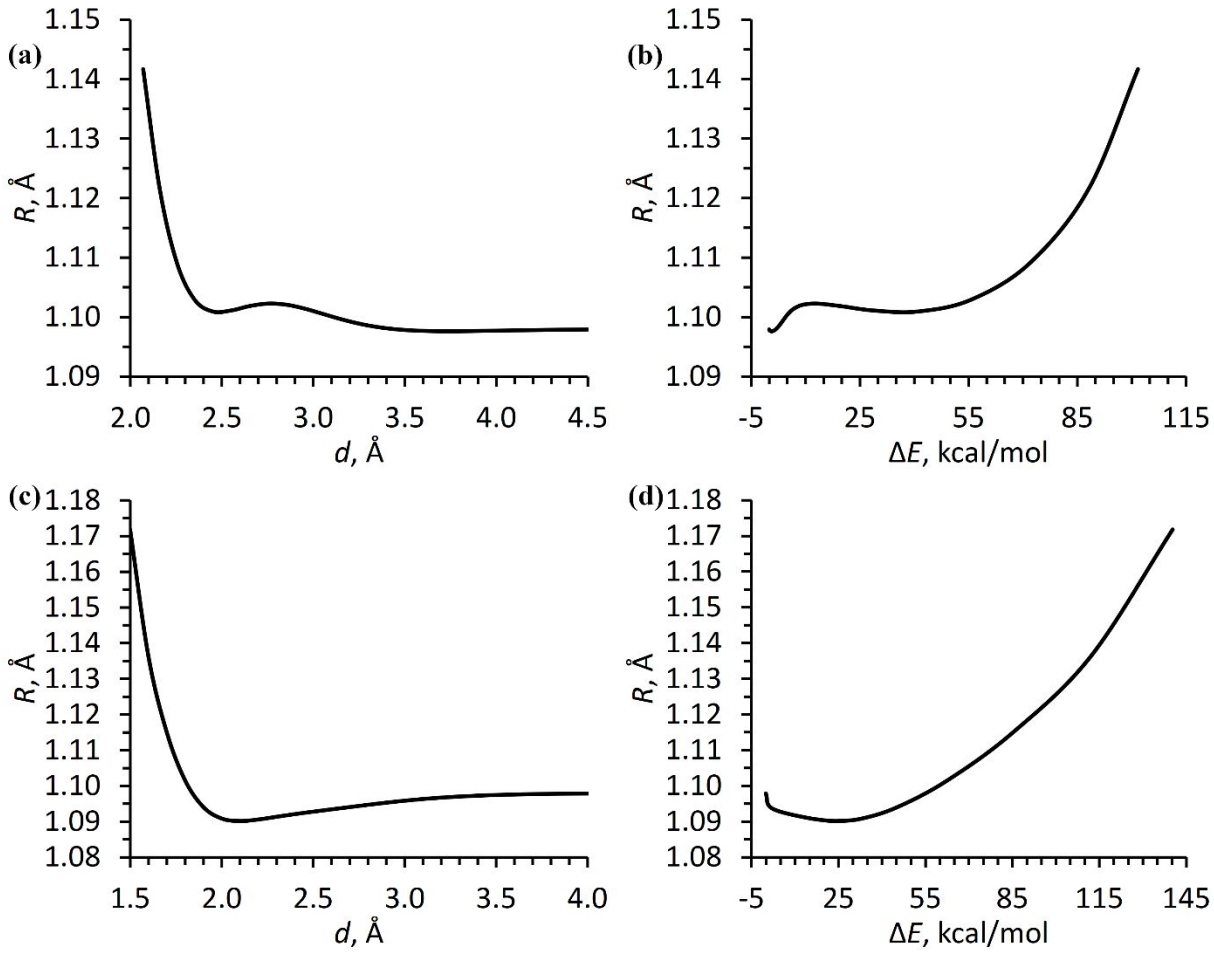

Figure 6. Optimal distances (*R*) of the diatomic molecule at fixed atom-diatom distances for different orientations in of $N_2(^1\Sigma_g^+)$ + N(^{4}S) collisions. (**a**) Collinear arrangement, and *R* is plotted vs. the distance (*d*) of third atom from the center of the diatomic molecule. (**b**) Collinear arrangement, and *R* is plotted vs. the relative potential energy. (**c**) Perpendicular arrangement, and *R* is plotted vs. *d*. (**d**) Perpendicular arrangement, and *R* is plotted vs. the relative potential energy.

In Fig. 7, we plot the force on the diatomic bond:

$$F = -\partial V/\partial R\big|_{R = 1.098\ \text{Å}} \tag{16}$$

as a function of *d* and ΔV for the collinear and perpendicular orientations. This provides an alternative route to gaining physical insight. For both collinear and perpendicular arrangements, when the diatom and the atom are well separated the force is close to zero (Figs. 7a and 7c). For the collinear arrangement (Fig. 7a and 7b), as the distance *d* decreases, the force increases. This is consistent with the increase of the optimum *R* in Fig. 6a. The changing slope of the force of Fig. 7a corresponds to the bump and well features of Fig. 6a for *d* = 3.2 – 2.4 Å. The forces in

the perpendicular arrangement (Figs. 7c and 7d) are also consistent with the discussion of Fig. 6. comparison of panels b and d is particularly informative. For the collinear approach (Fig. 7b), when the potential energy along the optimum path is between 55 and 100 kcal/mol, the force varies from 100 to 360 kcal mol^{-1} $Å^{-1}$; in contrast, for perpendicular-bisector approach, in the same 55-100 kcal/mol potential energy interval, the force is always between –30 and +25 kcal mol^{-1} $Å^{-1}$. Experience relating potential energy surface features to the probability of vibrational excitation[50] then allows us to infer that vibrational energy transfer should occur much more readily in high-energy collinear collisions than in high-energy perpendicular-bisector collisions.

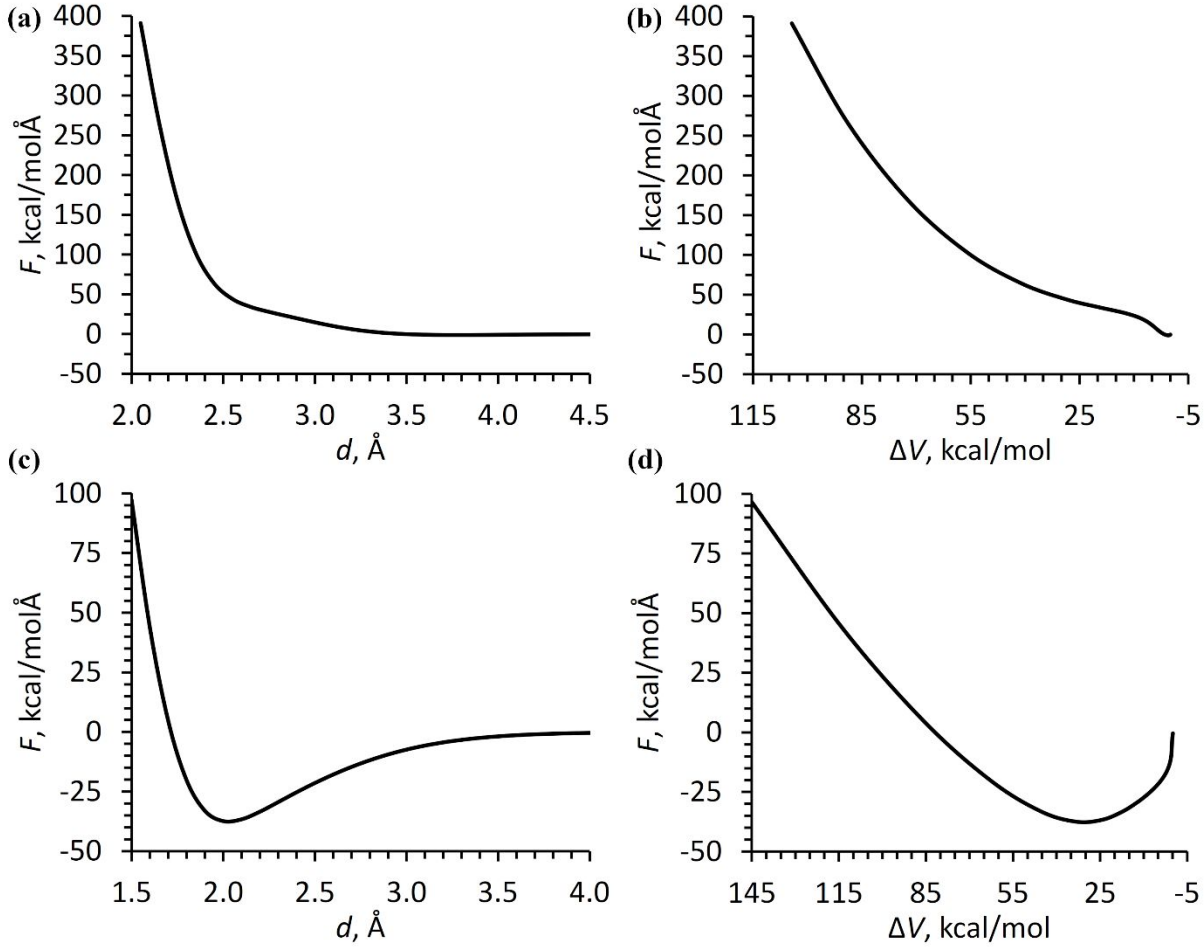

Figure 7. Forces on the diatomic bond in $N_2(^1\Sigma_g^+)$ + $N(^4S)$ collisions. (**a**) Collinear approach; force is plotted vs. the distance (*d*) of third atom from the center of the diatomic molecule. (**b**) Collinear approach; force is plotted vs. potential energy. (**c**) Perpendicular approach; force is plotted vs. *d*. (**d**) Perpendicular approach; force is plotted vs. potential energy.

4. Summary

In this article, we present an $N_3(^4A'')$ potential energy surface that is suitable of studying the high-energy electronically adiabatic collisions of $N_2(^1\Sigma_g^+)$ + N(^{4}S). This can be used for modeling chemical dynamics in shock waves. The 7,174 points in the data set for the fitting are based on CASPT2 calculations, and about 20% of them have an energy larger than 500 kcal/mol. The $N_2(^1\Sigma_g^+)$ diatomic potential of the current MB-PIP-MEG fit is used in other PESs of our group, and these PESs can be used together in direct molecular simulations[51,52,53,54] or master equation calculations (see for instance, refs 12, 13, 55, 56) to carry out multi-species hot air simulations.

We also showed that a three-body surface, which was obtained from a four-body ground-state surface by placing one of the atoms far apart from the other three, does not have the quartet spin state for the three-body subsystem at each geometry. Thus, such an approach is not suitable for generating a quartet potential energy surface for N_3.

Collision paths constrained to collinear and perpendicular atom arrangements were compared various ways. This includes collisions with stretched diatomic molecule to show the effect of vibrational excitation, optimized diatomic bond length sat various atom-diatom distances, and partial derivatives of the energy with respect to diatomic bond length at various atom-diatom distances or for various potential energies at the point of closest approach. The nonreactive approach of an N atom to N_2 along the perpendicular bisector is more repulsive than the collinear reproach, but plots of the force on the bond versus the potential energy at the distance of closest approach allow us to infer that vibrational energy transfer should occur much more readily in high-energy collinear collisions than in high-energy perpendicular-bisector collisions.

Conflicts of interest

There are no conflicts to declare.

Availability

The MB-PIP-MEG fit of the potential energy surfaces of $N_3(^4A'')$ is available in the electronic supplementary information, and it has been added to the online POTLIB library.[33,57]

Acknowledgments

Continuing discussions with Tom Schwartzentruber and Graham Candler are greatly appreciated. This work is supported by the Air Force Office of Scientific Research (grant no. FA9550-19-1-0219).

References

[1] A. Laganà, E. Garcia, and L. Ciccarelli, *J. Phys. Chem.*, 1978, **91**, 312.

[2] C. Petrongolo, *J. Mol. Struct.: THEOCHEM*, 1989, **202**, 135.

[3] P. Zhang, K. Morokuma, and A. M. Wodtke, *J. Chem. Phys.*, 2005, **122**, 014106.

[4] A. Laganà and E. Garcia, *J. Phys. Chem.*, 1994, **98**, 502.

[5] F. Esposito and M. Capitelli, *Chem. Phys. Lett.*, 1999, **302**, 49.

[6] S. Rampino, D. Skouteris, A. Laganà, E. Garcia, and A. Saracibar, *Phys. Chem. Chem. Phys.*, 2009, **11**, 1752.

[7] E. Garcia, A. Saracibar, A. Laganà, and D. Skouteris, *J. Phys. Chem. A*, 2007, **111**, 10362.

[8] A. Laganà, *J. Chem. Phys.*, 1991, **95**, 2216.

[9] A. Laganà, G. Ferraro, E. Garcia, O. Gervasi, and A. Ottavi, *Chem. Phys.*, 1992, **168**, 341.

[10] E. Garcia, A. Saracibar, S. Gómez-Carrasco, and A. Laganà, *Phys. Chem. Chem. Phys.*, 2008, **10**, 2552.

[11] D. Wang, J. R. Stallcop, W. M. Huo, C. E. Dateo, D. W. Schwenke, and H. Partridge, *J. Chem. Phys.*, 2003, **118**, 2186.

[12] G. Chaban, R. Jaffe, D. Schwenke, and W. Huo, AIAA 2008-1209. 46th AIAA Aerospace Sciences Meeting and Exhibit. January 2008.

[13] M. Panesi, R. L. Jaffe, D. Schwenke, and T. E. Magin, *J. Chem. Phys.*, 2013, **138**, 044312.

[14] Y. Wang, F. Meng, P. Yan, and D. Wang, *Chem. Phys. Lett.*, 2015, **633**, 202.

[15] B. R. L. Galvão and A. J. C. Varandas, *J. Phys. Chem. A*, 2009, **113**, 14424.

[16] T. K. Mankodi, U. V. Bhandarkar, and B. P. Puranik, *J. Chem. Phys.*, 2017, **146**, 204307.

[17] Y. Paukku, K. R. Yang, Z. Varga, and D. G. Truhlar, *J. Chem. Phys.*, 2013, **139**, 044309. Erratum: 2014, **140**, 019903.

[18] I. F. Galván, M. Vacher, A. Alavi, C. Angeli, F. Aquilante, J. Autschbach, J. J. Bao, S. I. Bokarev, N. A. Bogdanov, R. K. Carlson, L. F. Chibotaru, J. Creutzberg, N. Dattani, M. G. Delcey, S. S. Dong, A. Dreuw, L. Freitag, L. M. Frutos, L. Gagliardi, F. Gendron, A. Giussani, L. González, G. Grell, M. Guo, C. E. Hoyer, M. Johansson, S. Keller, S. Knecht, G. Kovačević, E. Källman, G. Li Manni, M. Lundberg, Y. Ma, S. Mai, J. P. Malhado, P. Å. Malmqvist, P. Marquetand, S. A. Mewes, J. Norell, M. Olivucci, M. Oppel, Q. M. Phung, K. Pierloot, F. Plasser, M. Reiher, A. M. Sand, I. Schapiro, P. Sharma, C. J. Stein, L. K. Sørensen, D. G. Truhlar, M. Ugandi, L. Ungur, A. Valentini, S. Vancoillie, V. Veryazov, O. Weser, T. A. Wesołowski, P.-O. Widmark, S. Wouters, A. Zech, J. P. Zobel, and R. Lindh, *J. Chem. Theory Comput.*, 2019, **15**, 5925.

[19] F. Aquilante, J. Autschbach, A. Baiardi, S. Battaglia, V. A. Borin, L. F. Chibotaru, I. Conti, L. De Vico, M. Delcey, I. F. Galván, N. Ferré, L. Freitag, M. Garavelli, X. Gong, S. Knecht, E. D. Larsson, R. Lindh, M. Lundberg, P. Å. Malmqvist, A. Nenov, J. Norell, M. Odelius, M. Olivucci, T. B. Pedersen, L. Pedraza-González, Q. M. Phung, K. Pierloot, M. Reiher, I. Schapiro, J. Segarra-Martí, F. Segatta, L. Seijo, S. Sen, D.-C. Sergentu, C. J. Stein, L. Ungur, M. Vacher, A. Valentini, and V. Veryazov, *J. Chem. Phys.*, 2020, **152**, 214117.

[20] E. Papajak, H. R. Leverentz, J. Zheng, and D. G. Truhlar, *J. Chem. Theory Comput.*, 2009, **5**, 1197.

[21] K. Ruedenberg, L. M. Cheung, and S. T. Elbert, *Int. J. Quantum Chem.*, 1979, **16**, 1069.

[22] B. O. Roos, P. R. Taylor, and P. E. M. Siegbahn, *Chem. Phys.*, 1980, **48** 157.

[23] B. O. Roos, *Adv. Chem. Phys.*, 1987, **69**, 399.

[24] K. Andersson, P.-Å. Malmqvist, B. O. Roos, A. Sadlej, and K. Wolinski, *J. Phys. Chem.*, 1990, **94** 5483.

[25] K. Andersson, P.-Å. Malmqvist, and B. O. Roos, *J. Chem. Phys.*, 1992, **96**, 1218.

[26] N. Forsberg and P.-Å. Malmqvist, *Chem. Phys. Lett.*, 1997, **274**, 196.

[27] F. B. Brown and D. G. Truhlar, *Chem. Phys. Lett.*, 1985, **117**, 307.

[28] D. G. Truhlar and J. T. Muckerman, Reactive Scattering Cross Sections III, in *Atom–Molecule Collision Theory*, edited by R. B. Bernstein, Plenum, New York, 1979, p. 505.

[29] J. Zheng, Z.-H. Li, A. W. Jasper, D. A. Bonhommeau, R. Valero, R. Meana-Pañeda, S. L. Mielke, L. Zhang, Z. Varga, and D. G. Truhlar, ANT, version 2020, University of Minnesota, Minneapolis, 2020, http://comp.chem.umn.edu/ant (accessed May 2021).

[30] Z. Varga, Y. Liu, J. Li, Y. Paukku, H. Guo, and D. G. Truhlar, *J. Chem. Phys.*, 2021 ,**154**, 084304.

[31] J. Li, Z. Varga, D. G. Truhlar, and H. Guo, *J. Chem. Theory Comput.*, 2020, **16**, 4822.

[32] J. D. Bender, P. Valentini, I. Nompelis, Y. Paukku, Z. Varga, D. G. Truhlar, T. Schwartzentruber, and G. V. Candler, *J. Chem. Phys.*, 2015, **143**, 054304.

[33] R. J. Duchovic, Y. L. Volobuev, G. C. Lynch, T. C. Allison, J. C. Corchado, D. G. Truhlar, A. F. Wagner, and B. C. Garrett, *Comput. Phys. Commun.*, 2002, **144**, 169. Erratum: 2004, **156**, 319.

[34] The updated singlet N_4 PES (N4_1A_MB-PIP-MEG3) is available in the updated POTLIB library at http://comp.chem.umn.edu/potlib/ (accessed June 2021).

[35] S. Grimme, J. Anthony, S. Ehrlich, and H. Krieg, *J. Chem. Phys.*, 2010, **132**, 154104.

[36] S. Grimme, S. Ehrlich, and L. Goerigk, *J. Comput. Chem.*, 2011, **32**, 1456.

[37] P. Verma, B. Wang, L. E. Fernandez, and D. G. Truhlar, *J. Phys. Chem. A*, 2017, **121**, 2855.

[38] B. J. Braams and J. M. Bowman, *Int. Rev. Phys. Chem.*, 2009, **28**, 577.

[39] Z. Xie and J. M. Bowman, *J. Chem. Theory Comput.*, 2010, **6**, 26.

[40] W. Lin, Z. Varga, G. Song, Y. Paukku, and D. G. Truhlar, *J. Chem. Phys.*, 2016, **144**, 024309.

[41] Z. Varga, Y. Paukku, and D. G. Truhlar, *J. Chem. Phys.*, 2017, **147**, 154312.

[42] K. R. Yang, Z. Varga, and D. G. Truhlar, PIPFit – version 2015, University of Minnesota, Minneapolis, 2015, https://comp.chem.umn.edu/pipfit/ (accessed June 2021).

[43] B. R. L. Galvão, P. J. S. B. Caridade, and A. J. C. Varandas, *J. Chem. Phys*, 2012, **137**, 22A515.

[44] C. J. Willmott and K. Matsuura, *Clim. Res.*, 2005, **30**, 79.

[45] P. J. Huber and E. M. Ronchetti, *Robust Statistics*,John Wiley & Sons, Inc.: Hoboken, NJ, USA, 2009.

[46] J. Zheng, S. Zhang, B. J. Lynch, J. C. Corchado, Y.-Y. Chuang, P. L. Fast, W.-P. Hu, Y.-P. Liu, G. C. Lynch, K. A. Nguyen, C. F. Jackels, A. Fernandez Ramos, B. A. Ellingson, V. S. Melissas, J. Villà, I. Rossi, E. L. Coitiño, J. Pu, T. V. Albu, R. Steckler, B. C. Garrett, A. D. Isaacson, and D. G. Truhlar, POLYRATE–version 2010–A, University of Minnesota, Minneapolis, 2010, https://comp.chem.umn.edu/polyrate/ (accessed June 2021).

[47] O. Tishchenko, J. Zheng, and D. G. Truhlar, *J. Chem. Theory Comput.*, 2008, **4**, 1208.

[48] D. G. Truhlar and M. S. Gordon, *Science*, 1990, **249**, 491.

[49] A. Kramida, Yu. Ralchenko, J. Reader, and NIST ASD Team (2015). NIST Atomic Spectra Database (ver. 5.3), [Online]. Available: http://physics.nist.gov/asd [2016, December 16]. National Institute of Standards and Technology, Gaithersburg, MD.

[50] J. W. Duff and D. G. Truhlar, *J. Chem. Phys.*, 1975, **63**, 4418.

[51] T. E. Schwartzentruber, M. S. Grover, and P. Valentini, *J. Thermophys. Heat Transfer*, 2018, **32**, 892.

[52] M. S. Grover, T. E. Schwartzentruber, Z. Varga, and D. G. Truhlar, *J. Thermophys. Heat Transfer*, 2019, **33**, 797.

[53] H. Luo, A. A. Alexeenko and S. O. Macheret, *AIAA Scitech 2020 Forum,* 2020*, **1**, Part F,* 1.

[54] J. Arnold, D. Koner, S. Käser, N. Singh, R. J. Bemish and M. Meuwly, M. *J. Phys. Chem. A,*2020, **124**, 7177.

[55] R. Jaffe, D. Schwenke and G. Chaban, AIAA 2009-1569. 47th AIAA Aerospace Sciences Meeting including The New Horizons Forum and Aerospace Exposition. January 2009.

[56] J. G. Kim and I. D. Boyd, *Chem. Phys.*, 2013, **415**, 237.

[57] The $N_3(^4A'')$ PES (N3_4App_MB-PIP-MEG) is available in the POTLIB library at http://comp.chem.umn.edu/potlib/ (accessed June 22, 2021)